

Article

Low-Resolution Precoding for Multi-Antenna Downlink Channels and OFDM †

Andrei Stefan Nedelcu ¹, Fabian Steiner ² and Gerhard Kramer ^{2,*} 

¹ Optical and Quantum Laboratory, Huawei Munich Research Center, 80992 Munich, Germany; andrei.nedelcu2@huawei.com

² Institute for Communications Engineering, Technical University of Munich (TUM), 80333 Munich, Germany; fabian.steiner@tum.de

* Correspondence: gerhard.kramer@tum.de

† The results of this paper have been presented in part at the Workshop on Smart Antennas (WSA) 2018.

Abstract: Downlink precoding is considered for multi-path multi-input single-output channels where the base station uses orthogonal frequency-division multiplexing and low-resolution signaling. A quantized coordinate minimization (QCM) algorithm is proposed and its performance is compared to other precoding algorithms including squared infinity-norm relaxation (SQUID), multi-antenna greedy iterative quantization (MAGIQ), and maximum safety margin precoding. MAGIQ and QCM achieve the highest information rates and QCM has the lowest complexity measured in the number of multiplications. The information rates are computed for pilot-aided channel estimation and a blind detector that performs joint data and channel estimation. Bit error rates for a 5G low-density parity-check code confirm the information-theoretic calculations. Simulations with imperfect channel knowledge at the transmitter show that the performance of QCM and SQUID degrades in a similar fashion as zero-forcing precoding with high resolution quantizers.

Keywords: massive MIMO; precoding; coarse quantization; coordinate descent; information rates



Citation: Nedelcu, A.S.; Steiner, F.; Kramer, G. Low-Resolution Precoding for Multi-Antenna Downlink Channels and OFDM. *Entropy* **2022**, *24*, 504. <https://doi.org/10.3390/e24040504>

Academic Editor: Syed A. Jafar

Received: 13 February 2022

Accepted: 27 March 2022

Published: 4 April 2022

Publisher's Note: MDPI stays neutral with regard to jurisdictional claims in published maps and institutional affiliations.



Copyright: © 2022 by the authors. Licensee MDPI, Basel, Switzerland. This article is an open access article distributed under the terms and conditions of the Creative Commons Attribution (CC BY) license (<https://creativecommons.org/licenses/by/4.0/>).

1. Introduction

Massive multiple-input multiple-output (MIMO) base stations can serve many user equipments (UEs) with high spectral efficiency and simplified signal processing [1,2]. However, their implementation is challenging due to the cost and energy consumption of analog-to-digital and digital-to-analog converters (ADCs/DACs) and linear power amplifiers (PAs). There are several approaches to lower cost. One approach is hybrid beamforming with analog beamformers in the radio frequency (RF) chain of each antenna and where the digital baseband processing is shared among RF chains. Second, constant envelope waveforms permit using non-linear PAs. Third, all-digital approaches use low-resolution ADCs/DACs or low-resolution digitally controlled RF chains. The focus of this paper is on the all-digital approach.

1.1. Single-Carrier Transmission

We study the multi-antenna downlink and UEs with one antenna each, a model referred to as multi-user multi-input single-output (MU-MISO). Most works on low-cost precoding for MU-MISO consider phase-shift keying (PSK) to lower the requirements on the PAs. For instance, the early papers [3,4] (see also [5]) use iterative coordinate-wise optimization to choose transmit symbols from a continuous PSK alphabet for flat and frequency-selective (or multipath) fading, respectively. We remark that these papers do not include an optimization parameter (called α below, see (8)) in their cost function, which plays an important role at high signal-to-noise ratio (SNR), see [6,7]. This parameter is related to linear minimum-mean square error (MMSE) precoding.

Most works consider discrete alphabet signaling. Perhaps the simplest approach, called quantized linear precoding (QLP), applies a linear precoder followed by one low-resolution quantizer per antenna [8–15]. Our focus is on zero forcing (ZF), and we use the acronyms LP-ZF and QLP-ZF, respectively, for unquantized ZF and the QLP version of ZF.

More sophisticated approaches use optimization tools as in [3,4]. For example, the papers [16–18] use convex relaxation methods; Refs. [19–25] apply coordinate-wise optimization; Refs. [26–28] develops a symbol-wise Maximum Safety Margin (MSM) precoder; Refs. [29–32] use a branch-and-bound (BB) algorithm; Ref. [33] uses a majorization-minimization algorithm; Ref. [34] uses integer programming; and [35,36] use neural networks (NNs). These references are collected in Table 1 together with the papers listed below on orthogonal frequency-division multiplexing (OFDM). As the table shows, most papers focus on single-carrier and flat fading channels.

Table 1. References for quantized precoding.

Modulation	Fading	Precoding Algorithm			
		QLP	Convex Relaxation	Coord.-Wise Optimization	Other (MSM, BB, NN, etc.)
1 Carrier	Flat Freq.-Sel.	[8–15]	[16–18]	[19–25]	[26,27,29–36] [28]
OFDM	Freq.-Sel.	[37]	[38]	[39–41]	[42,43]

1.2. Discrete Signaling and OFDM

Our main interest is discrete-alphabet precoding for multipath channels with OFDM as in 5G wireless systems. Precoding for OFDM is challenging because the alphabet constraint is in the time domain after the inverse discrete Fourier transform (IDFT) rather than in the frequency domain. We further focus on using information theory to derive achievable rates. For this purpose, we consider two types of receivers: classic pilot-aided transmission (PAT) and a blind detector that performs joint data and channel estimation.

Discrete-alphabet precoding for OFDM was treated in Ref. [37], who used QLP and low resolution DACs. A more sophisticated approach appeared in Ref. [38], who applied a squared-infinity norm Douglas-Rachford splitting (SQUID) algorithm to minimize a quadratic cost function in the frequency domain. The performance was illustrated via bit error rate (BER) simulations with convolutional codes and QPSK or 16-quadrature amplitude modulation (QAM) by using 1–3 bits of phase quantization.

The paper [39] instead proposed an algorithm called multi-antenna greedy iterative quantization (MAGIQ) that builds on [19] and uses coordinate-wise optimization of a quadratic cost function in the time domain. MAGIQ may thus be considered an extended version of [4] for OFDM and discrete alphabets. Simulations showed that MAGIQ outperforms SQUID in terms of complexity and achievable rates. Another coordinate-wise optimization algorithm appeared in [40,41] that builds on the papers [21,22]. The algorithm is called constant envelope symbol level precoding (CESLP) and it is similar to the refinement of MAGIQ presented here. The main difference is that, as in [38], the optimization in [40,41] uses a cost function in the frequency domain rather than the time domain. We remark that processing in the time domain has advantages that are described in Section 3.1.

The MSM algorithm was extended to OFDM in [42]. MSM works well at low and intermediate rates but MAGIQ outperforms MSM at high rates both in terms of complexity and achievable rates. Finally, the recent paper [43] uses generalized approximate message passing (GAMP) for OFDM.

1.3. Contributions and Organization

The contributions of this paper are as follows.

- The analysis of MAGIQ in the workshop paper [39] is extended to larger systems and more realistic channel conditions;
- Replacing the greedy antenna selection rule of MAGIQ with a fixed (round-robin) schedule is shown to cause negligible rate loss. The new algorithm is named quantized coordinate minimization (QCM);
- The performance of QLP-ZF, SQUID, MSM, MAGIQ, and QCM are compared in terms of complexity (number of multiplications and iterations) and achievable rates;
- We develop an auxiliary channel model to compute achievable rates for pilot-aided channel estimation and a blind detector that performs joint channel and data estimation. The models let one compare modulations, precoders, channels, and receivers;
- Simulations with a 5G NR low-density parity-check (LDPC) code [44] show that the computed rate and power gains accurately predict the gains of standard channel codes;
- Simulations with imperfect channel knowledge at the base station show that the achievable rates of SQUID and QCM degrade as gracefully as those of LP-ZF.

We remark that our focus is on algorithms that approximate ZF based on channel inversion, i.e., there is no attempt to optimize transmit powers across subcarriers. This approach simplifies OFDM channel estimation at the receivers because the precoder makes all subcarriers have approximately the same channel magnitude and phase. For instance, a rapid and accurate channel estimate is obtained for each OFDM symbol by averaging the channel estimates of the subcarriers, see Section 4.1. Of course, it is interesting to develop algorithms for other precoders and for subcarrier power allocation.

This paper is organized as follows. Section 2 introduces the baseband model and OFDM signaling. Section 3 describes the MAGIQ and QCM precoders. Section 4 develops theory for achievable rates, presents complexity comparisons, and reviews a model for imperfect channel state information (CSI). Section 5 compares achievable rates and BERs with 5G NR LDPC codes. Section 6 concludes the paper.

2. System Model

Figure 1 shows a MU-MISO system with N transmit antennas and K UEs that each have a single antenna. The base station has one message per UE and each antenna has a resolution of 1 bit for the amplitude (on-off switch) and b bits for the phase per antenna. All other hardware components are ideal: linear, infinite bandwidth, no distortions except for additive white Gaussian noise (AWGN).

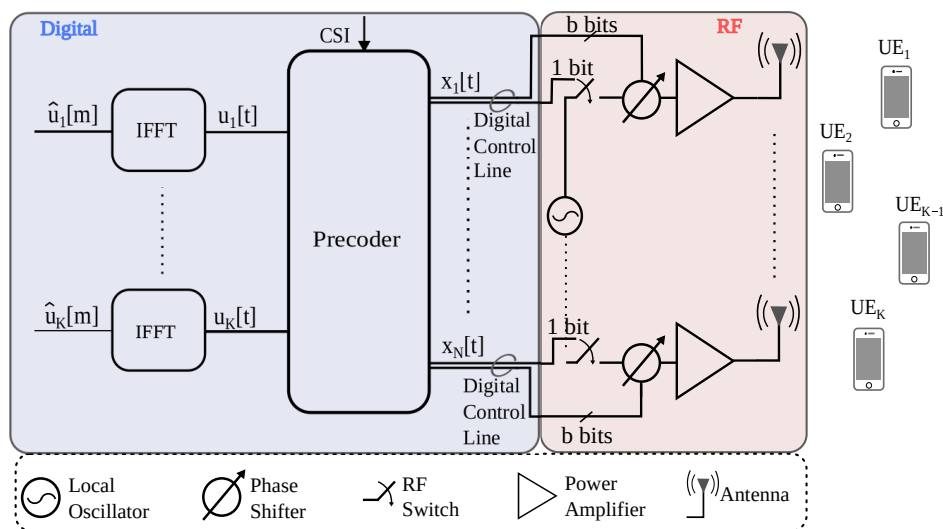


Figure 1. Multi-user MIMO downlink with a low resolution digitally controlled analog architecture.

2.1. Baseband Channel Model

The discrete-time baseband channel is modeled as a finite impulse response filter between each pair of transmit and receive antennas. Let $x_n[t]$ be the symbol of transmit antenna n at time t and let $\mathbf{x}[t] = (x_1[t] \dots x_N[t])^T$. Similarly, let $y_k[t]$ be the received symbol of UE k at time t and let $\mathbf{y}[t] = (y_1[t] \dots y_K[t])^T$. The channel model is

$$\mathbf{y}[t] = \sum_{\tau=0}^{L-1} \mathbf{H}[\tau] \mathbf{x}[t - \tau] + \mathbf{z}[t] \tag{1}$$

where the noise $\mathbf{z}[t] = (z_1[t] \dots z_K[t])^T$ has circularly-symmetric, complex, Gaussian entries that are independent and have variance σ^2 , i.e., we have $\mathbf{z} \sim \mathcal{CN}(\mathbf{0}, \sigma^2 \mathbf{I})$. The $\mathbf{H}[\tau]$, $\tau = 0, \dots, L - 1$, are $K \times N$ matrices representing the channel impulse response, i.e., we have

$$\mathbf{H}[\tau] = \begin{pmatrix} h_{11}[\tau] & h_{12}[\tau] & \dots & h_{1N}[\tau] \\ h_{21}[\tau] & h_{22}[\tau] & \dots & h_{2N}[\tau] \\ \vdots & \vdots & \ddots & \vdots \\ h_{K1}[\tau] & h_{K2}[\tau] & \dots & h_{KN}[\tau] \end{pmatrix} \tag{2}$$

where $h_{kn}[\cdot]$ is the channel impulse response from the n -th antenna at the base station to the k -th UE. For instance, a Rayleigh fading multi-path channel with a uniform power delay profile (PDP) has $h_{kn}[\tau] \sim \mathcal{CN}(0, 1/L)$ and these taps are independent and identically distributed (iid) for all k, n, τ .

The vector $\mathbf{x}[t]$ is constrained to have entries taken from a discrete and finite alphabet

$$\mathcal{X} = \{0\} \cup \left\{ \sqrt{\frac{P}{N}} e^{j2\pi q/2^b}; q = 0, 1, 2, \dots, 2^b - 1 \right\}. \tag{3}$$

The transmit energy clearly satisfies $\|\mathbf{x}[t]\|^2 \leq P$ and we define $\text{SNR} = P/\sigma^2$. The inequality is due to the 0 symbol that permits antenna selection. Antenna selection was also used in [45] to enforce sparsity. Our intent is rather to allow antennas not to be used if they do not improve performance.

2.2. OFDM Signaling

Figure 1 shows how OFDM can be combined with the precoder. Let $T = T_F + T_c$ be the OFDM blocklength with T_F symbols for the DFT and T_c symbols for the cyclic prefix. We assume that $T_F \geq L$ and $T_c \geq L - 1$. For simplicity, all T_F subcarriers carry data and we do not include the cyclic prefix overhead in our rate calculations below, i.e., the rates in bits per channel use (bpcu) are computed by normalizing by T_F .

Consider the frequency-domain modulation alphabet $\hat{\mathcal{U}}$ that has a finite number of elements, e.g., QPSK has $\hat{\mathcal{U}} = \{\hat{u} : \hat{u} = (\pm 1 \pm j)/\sqrt{2}\}$. Messages are mapped to the frequency-domain vectors $\hat{\mathbf{u}}[m] = (\hat{u}_1[m], \dots, \hat{u}_K[m])^T$ for subcarriers $m = 0, \dots, T_F - 1$ that are converted to time-domain vectors $\mathbf{u}[t]$ by IDFTs

$$u_k[t] = \frac{1}{T_F} \sum_{m=0}^{T_F-1} \hat{u}_k[m] e^{j2\pi mt/T_F} \tag{4}$$

for times $t = 0, \dots, T_F - 1$ and UEs $k = 1, \dots, K$. For the simulations below, we generated the $\hat{u}_k[m]$ uniformly from finite constellations such as 16-QAM or 64-QAM. We assume that $E[\hat{u}_k[m]] = 0$ for all k and m . Each UE k uses a DFT to convert its time-domain symbols $y_k[t]$ to the frequency-domain symbols

$$\hat{y}_k[m] = \sum_{t=0}^{T_F-1} y_k[t] e^{-j2\pi mt/T_F}. \tag{5}$$

2.3. Linear MMSE Precoding

To describe the linear MMSE precoder, consider the channel from base station antenna n to UE k :

$$\mathbf{h}_{kn} = (h_{kn}[0], \dots, h_{kn}[L-1], \underbrace{0, \dots, 0}_{(T_F - L) \text{ zeros}})^T \tag{6}$$

and denote its DFT as $\hat{\mathbf{h}}_{kn} = (\hat{h}_{kn}[0], \dots, \hat{h}_{kn}[T_F - 1])^T$. The channel of subcarrier m is the $K \times N$ matrix $\hat{\mathbf{H}}[m]$ with entries $\hat{h}_{kn}[m]$ for $k = 1, \dots, K, n = 1, \dots, N$. The linear MMSE precoder (or Wiener filter) for subcarrier m is

$$P[m]\hat{\mathbf{H}}[m]^\dagger \left(P[m]\hat{\mathbf{H}}[m]\hat{\mathbf{H}}[m]^\dagger + \sigma^2\mathbf{I} \right)^{-1} \tag{7}$$

where $P[m] = E[|\hat{u}_k[m]|^2]$ is the same for all k , $\hat{\mathbf{H}}[m]^\dagger$ is the Hermitian of $\hat{\mathbf{H}}[m]$, and \mathbf{I} is the $K \times K$ identity matrix. The precoder multiplies $\hat{\mathbf{u}}[m]$ by (7) for all subcarriers m , and performs N IDFTs to compute the resulting $\mathbf{x}[0], \dots, \mathbf{x}[T_F - 1]$. We remark that ZF precoding is the same as (7) but with $\sigma^2 = 0$, where $\hat{\mathbf{H}}[m]\hat{\mathbf{H}}[m]^\dagger$ is usually invertible if N is much larger than K .

3. Quantized Precoding

We wish to ensure compatibility with respect to LP-ZF. In other words, each receiver k should ideally see signals $u_k[t], t = 0, \dots, T - 1$, that were generated from the frequency-domain signals $\hat{u}_k[m], m = 0, \dots, T_F - 1$. Let $\mathbf{u}[t] = (u_1[t] \dots u_K[t])^T$ and define the time-domain mean square error (MSE) cost function

$$\begin{aligned} G(\mathbf{x}[0], \dots, \mathbf{x}[T-1], \alpha) &= \sum_{t=0}^{T-1} E_{z[t]} \left[\|\mathbf{u}[t] - \alpha \mathbf{y}[t]\|^2 \right] \\ &= \sum_{t=0}^{T-1} \left\| \mathbf{u}[t] - \alpha \sum_{\tau=0}^{L-1} \mathbf{H}[\tau] \mathbf{x}[t-\tau] \right\|^2 + \alpha^2 TK\sigma^2 \end{aligned} \tag{8}$$

where $E_{z[t]}[\cdot]$ denotes the expectation with respect to the noise $\mathbf{z}[t]$. The optimization problem is as follows:

$$\begin{aligned} \min_{\mathbf{x}[0], \dots, \mathbf{x}[T-1], \alpha} \quad & G(\mathbf{x}[0], \dots, \mathbf{x}[T-1], \alpha) \\ \text{s.t.} \quad & \mathbf{x}[t] \in \mathcal{X}^N, t = 0, \dots, T-1 \\ & \alpha > 0. \end{aligned} \tag{9}$$

The parameter α in (8) and (9) can easily be optimized for fixed $\mathbf{x}[0], \dots, \mathbf{x}[T-1]$ and the result is (see [18] Equation (26))

$$\alpha = \frac{\sum_{t=0}^{T-1} \text{Re} \left(\mathbf{u}[t]^H \sum_{\tau=0}^{L-1} \mathbf{H}[\tau] \mathbf{x}[t-\tau] \right)}{\sum_{t=0}^{T-1} \left\| \sum_{\tau=0}^{L-1} \mathbf{H}[\tau] \mathbf{x}[t-\tau] \right\|^2 + TK\sigma^2}. \tag{10}$$

For the MAGIQ and QCM algorithms below, we use alternating minimization to find the $\mathbf{x}[0], \dots, \mathbf{x}[T-1]$ and α . For the linear MMSE precoder, we label the α in (10) as α_{WF} .

Observe that we use the same α for all K UEs because all UEs experience the same shadowing, i.e., all K UEs see the same average power. For UE-dependent shadowing, a more general approach would be to replace α with a diagonal matrix with K parameters $\alpha_k, k = 1, \dots, K$, and then modify (8) appropriately.

3.1. MAGIQ and QCM

For multipath channels, the vector $\mathbf{x}[t]$ influences the channel output at times $t, t + 1, \dots, t + L - 1$. A joint optimization over strings of length T seems difficult because of this influence and because of the finite alphabet constraint for the $x_n[t]$. Instead, MAGIQ splits the optimization into sub-problems with reduced complexity by applying coordinate-wise minimization across the antennas and iterating over the OFDM symbol.

For this purpose, consider the precoding problem for time t' starting at $t' = 0$ and ending at $t' = T - 1$. Observe that $\mathbf{x}[t']$ influences at most L summands in (8), namely the summands for $t = (t')_T, \dots, (t' + L - 1)_T$ where $(t)_T = \min(t, T - 1)$. To compute the new cost after updating the symbol $x_n[t']$, one may thus compute sums of the form

$$\sum_{t=(t')_T, \dots, (t'+L-1)_T} \left\| \mathbf{u}[t] - \alpha \sum_{\tau=0}^{L-1} \mathbf{H}[\tau] \mathbf{x}[t - \tau] \right\|^2 \quad (11)$$

for $t' = 0, \dots, T - 1$. In both cases, one computes a first and second sum having the old and new $x_n[t']$, respectively. One then takes the difference and adds the result to (8) to obtain the updated cost.

We remark that the time-domain cost function (8) is closely related to the frequency-domain cost functions in [38,40,41]. However, the time-domain approach is more versatile as it can include acyclic phenomena such as interference from previous OFDM blocks. The time-domain approach is also slightly simpler because updating the symbol $x_n[t']$ in (8) or (11) requires taking the norm of at most L vectors of dimension K for each test symbol in \mathcal{X} while the frequency-domain approach in ([40] Equation (17)) takes the norm of T_F vectors of dimension K for each test symbol. Recall that $T_F \geq L$, and usually $T_F \geq 10L$ to avoid losing too much efficiency with the cyclic prefix that has length $T_c \geq L - 1$.

The MAGIQ algorithm is summarized in Algorithm 1. MAGIQ steps through time in a cyclic fashion for fixed α . At each time t , it initializes the antenna set $\mathcal{S} = \{1, \dots, N\}$ and performs a greedy search for the antenna n and symbol $x_n[t]$ that minimize (8) (one may equivalently consider sums of L norms as in (11)). The resulting antenna is removed from \mathcal{S} and a new greedy search is performed to find the antenna in the new \mathcal{S} and the symbol that minimizes (8) while the previous symbol assignments are held fixed. This step is repeated until \mathcal{S} is empty. MAGIQ then moves to the next time and repeats the procedure. To determine α , MAGIQ applies alternating minimization with respect to α and the precoder output $\{\mathbf{x}[t] : t = 0, \dots, T - 1\}$. For fixed $\mathbf{x}[\cdot]$ the minimization can be solved in closed form, see (10) and line 22 of Algorithm 1.

Simulations show that MAGIQ exhibits good performance and converges quickly [39]. However, the greedy selection considerably increases the computational complexity. We thus replace the minimization over \mathcal{S} in line 9 of Algorithm 1) with a round-robin schedule or a random permutation. We found that both approaches perform equally well. The new QCM algorithm performs as well as MAGIQ but with a simpler search and a small increase in the number of iterations.

Finally, one might expect that α is close to the α_{WF} of the transmit Wiener filter [6,7] since our cost function accounts for the noise power. However, Figure 2 shows that this is true only at low SNR. The figure plots the average α of the QCM algorithm, called α_{QCM} , against the computed α_{WF} for simulations with System A in Section 5. Note that α_{QCM} is generally larger than α_{WF} .

Algorithm 1 MAGIQ and QCM precoding.

```

1: procedure PRECODE(Algo,  $H[\cdot]$ ,  $u[\cdot]$ )
2:    $\mathbf{x}^{(0)}[\cdot] = \mathbf{x}[\cdot]_{init}$ 
3:    $\alpha^{(0)} = \alpha_{init}$ 
4:   for  $i = 1 : I$  do // iterate over OFDM block
5:     for  $t = 0 : T - 1$  do
6:        $\mathcal{S} = \{1, \dots, N\}$ 
7:       while  $\mathcal{S} \neq \emptyset$  do
8:         if Algo = MAGIQ then
9:            $(x_{n^*}^*, n^*) = \operatorname{argmin}_{\tilde{x}_n \in \mathcal{X}, n \in \mathcal{S}}$ 
10:             $G(\mathbf{x}^{(i)}[0], \dots, \mathbf{x}^{(i)}[t-1], \tilde{\mathbf{x}},$ 
11:               $\mathbf{x}^{(i-1)}[t+1], \dots, \mathbf{x}^{(i-1)}[T-1], \alpha^{(i-1)})$ 
12:         else // Algo = QCM
13:            $n^* = \min \mathcal{S}$  // round-robin schedule
14:            $x_{n^*}^* = \operatorname{argmin}_{\tilde{x}_{n^*} \in \mathcal{X}}$ 
15:             $G(\mathbf{x}^{(i)}[0], \dots, \mathbf{x}^{(i)}[t-1], \tilde{\mathbf{x}},$ 
16:               $\mathbf{x}^{(i-1)}[t+1], \dots, \mathbf{x}^{(i-1)}[T-1], \alpha^{(i-1)})$ 
17:         end if
18:          $x_{n^*}^{(i)}[t] = x_{n^*}^*$  // update antenna  $n^*$  at time  $t$ 
19:          $\mathcal{S} \leftarrow \mathcal{S} \setminus \{n^*\}$ 
20:       end while
21:     end for
22:      $\alpha^{(i)} = \frac{\sum_{t=0}^{T-1} \operatorname{Re}(u[t]^H \sum_{\tau=0}^{L-1} H[\tau] x^{(i)}[t-\tau])}{\sum_{t=0}^{T-1} \|\sum_{\tau=0}^{L-1} H[\tau] x^{(i)}[t-\tau]\|^2 + TK\sigma^2}$ 
23:   end for
24:   return  $\mathbf{x}[\cdot] = \mathbf{x}^{(I)}[\cdot]$ ,  $\alpha = \alpha^{(I)}$ 
25: end procedure

```

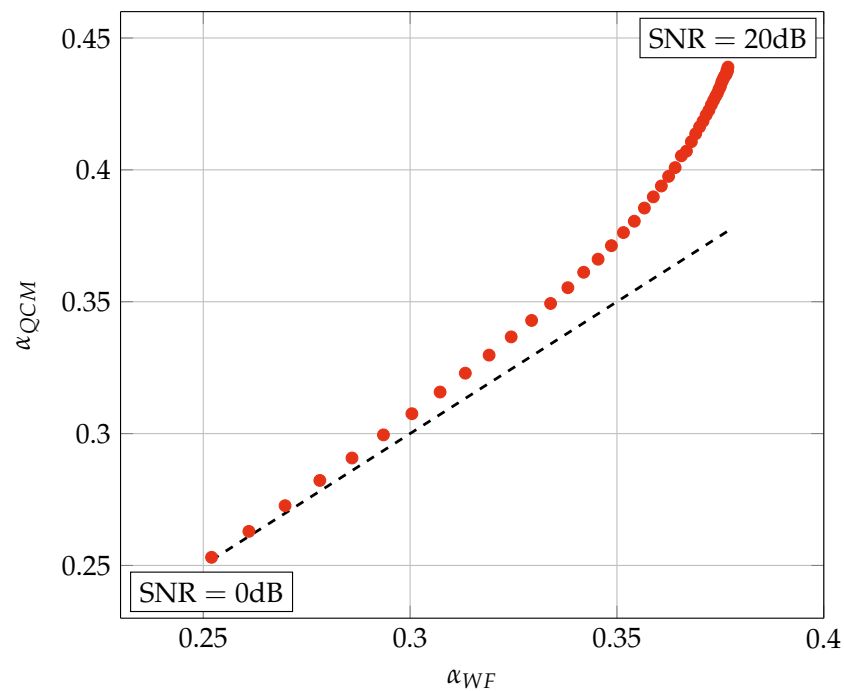


Figure 2. α_{QCM} vs. α_{WF} for System A of Table 2 and 64-QAM.

Table 2. System parameters for the simulations.

System	N	K	$T = T_F + T_c$	L	Constellation	b	Fading Statistics
A	128	16	270 = 256 + 14	15	{16, 64}-QAM	2, 3	Flat and Rayleigh uniform PDP
B	64	8	35 = 32 + 3	4	{4-32}-PSK	2	Rayleigh uniform PDP
C	80	8	277 = 256 + 21 286 = 256 + 30	22 varies	16-QAM	2	Rayleigh uniform PDP Winner2 NLOS C2 urban
D	128	16	410 = 396 + 14	15	64-QAM	2	Rayleigh uniform PDP

4. Performance Metrics

4.1. Achievable Rates

We use generalized mutual information (GMI) to compute achievable rates [46,47], (Ex. 5.22) which is a standard tool to compare coded systems. Consider a generic input distribution $P(x)$ and a generic channel density $p(y|x)$ where $x = (x_1, \dots, x_S)^T$ and $y = (y_1, \dots, y_S)^T$ each have S symbols. A lower bound to the mutual information

$$I(X; Y) = \sum_{x,y} P(x)p(y|x) \log_2 \left(\frac{p(y|x)}{\sum_a P(a)p(y|a)} \right) \tag{12}$$

is the GMI

$$I_{q,s}(X; Y) = \sum_{x,y} P(x)p(y|x) \log_2 \left(\frac{q(y|x)^s}{\sum_a P(a)q(y|a)^s} \right) \tag{13}$$

where $q(y|x)$ is any auxiliary density and $s \geq 0$. In other words, the choices $q(y|x) = p(y|x)$ for all x, y and $s = 1$ maximize the GMI. However, the idea is that $p(y|x)$ may be unknown or difficult to compute and so one chooses a simple $q(y|x)$. The reason why $p(y|x)$ is difficult to compute here is because we will measure the GMI across the end-to-end channels from the $\hat{u}_k[m]$ to the $\hat{y}_k[m]$ and the quantized precoding introduces non-linearities in these channels. The final step in evaluating the GMI is maximizing over $s \geq 0$. Alternatively, one might wish to simply focus on $s = 1$, e.g., see [48].

We study the GMI of two non-coherent systems: classic PAT and a blind detector that performs joint data and channel estimation. For both systems, we apply memoryless signaling with the product distribution

$$P(x) = \prod_{i=1}^{S_p} 1(x_i = x_{p,i}) \cdot \prod_{i=S_p+1}^S P(x_i) \tag{14}$$

where the $x_{p,i}$ are pilot symbols, $1(a = b)$ is the indicator function that takes on the value 1 if its argument is true and 0 otherwise, and $P(x)$ is a uniform distribution. Joint data and channel estimation has $S_p = 0$ so that we have only the second product in (14). At the receiver we use the auxiliary channel

$$q(y|x) = \prod_{i=1}^S q_{x,y}(y_i | x_i) \tag{15}$$

where the symbol channel $q_{x,y}(\cdot)$ is a function of x and y . Observe that $q_{x,y}(\cdot)$ is invariant for S symbols and the channel can be considered to have memory since every symbol x_ℓ

or $y_\ell, \ell = 1, \dots, S$, influences the channel for all “times” $i = 1, \dots, S$. The GMI rate (13) simplifies to

$$\sum_{\mathbf{x}, \mathbf{y}} P(\mathbf{x}) p(\mathbf{y}|\mathbf{x}) \sum_{i=S_p+1}^S \log_2 \left(\frac{q_{\mathbf{x}, \mathbf{y}}(y_i | x_i)^s}{\sum_a P(a) q_{\mathbf{x}, \mathbf{y}}(y_i | a)^s} \right). \tag{16}$$

One may approximate (16) by applying the law of large numbers for stationary signals and channels. The idea is to independently generate the B pairs of vectors

$$\begin{aligned} \mathbf{x}^{(b)} &= (x_1^{(b)}, \dots, x_S^{(b)})^T \\ \mathbf{y}^{(b)} &= (y_1^{(b)}, \dots, y_S^{(b)})^T \end{aligned}$$

for $b = 1, \dots, B$, and then the following average rate will approach $I_{q,s}(\mathbf{X}; \mathbf{Y})/S$ bpcu as B grows:

$$R_a = \frac{1}{B} \sum_{b=1}^B R_a^{(b)} \tag{17}$$

where

$$R_a^{(b)} = \frac{1}{S} \sum_{i=S_p+1}^S \log_2 \left(\frac{q_{\mathbf{x}^{(b)}, \mathbf{y}^{(b)}}(y_i^{(b)} | x_i^{(b)})^s}{\sum_a P(a) q_{\mathbf{x}^{(b)}, \mathbf{y}^{(b)}}(y_i^{(b)} | a)^s} \right). \tag{18}$$

We choose the Gaussian auxiliary density

$$q_{\mathbf{x}, \mathbf{y}}(y|x) = \frac{1}{\pi \sigma_q^2} \exp \left(-\frac{|y - h \cdot x|^2}{\sigma_q^2} \right) \tag{19}$$

where for PAT the receiver computes joint maximum likelihood (ML) estimates with sums of S_p terms:

$$\begin{aligned} h &= \frac{\sum_{i=1}^{S_p} y_i \cdot x_i^*}{\sum_{i=1}^{S_p} |x_i|^2} \\ \sigma_q^2 &= \frac{1}{S_p} \sum_{i=1}^{S_p} |y_i - h \cdot x_i|^2. \end{aligned} \tag{20}$$

For the blind detector we replace S_p with S in (20). Note that for the Gaussian channel (19) the parameter s multiplies $1/\sigma_q^2$ in (16) or (18), and optimizing s turns out to be the same as choosing the best parameter σ_q^2 when $s = 1$.

Summarizing, we use the following steps to evaluate achievable rates. Suppose the coherence time is S/T_F OFDM symbols where S is a multiple of T_F . We index the channel symbols by the pairs (ℓ, m) where ℓ is the OFDM symbol and m is the subcarrier, $1 \leq \ell \leq S/T_F, 0 \leq m \leq T - 1$. We collect the pilot index pairs in the set \mathcal{S}_p that has cardinality S_p , and we write the channel inputs and outputs of UE k for OFDM symbol ℓ and subcarrier m as $\hat{u}_k[\ell, m]$ and $\hat{y}_k[\ell, m]$, respectively.

1. Repeat the following steps (2)–(4) B times; index the steps by $b = 1, \dots, B$;
2. Use Monte Carlo simulation to generate the symbols $\hat{u}_k[\ell, m]$ and $\hat{y}_k[\ell, m]$ for $k = 1, \dots, K, \ell = 1, \dots, S/T_F$, and $m = 0, \dots, T - 1$;

- Each UE estimates its own channel h_k and $\sigma_{q,k}^2$, i.e., the channel estimate (20) of UE k is

$$h_k = \frac{\sum_{(\ell,m) \in \mathcal{S}_p} \hat{y}_k[\ell, m] \cdot \hat{u}_k[\ell, m]^*}{\sum_{(\ell,m) \in \mathcal{S}_p} |\hat{u}_k[\ell, m]|^2} \tag{21}$$

$$\sigma_{q,k}^2 = \frac{1}{S_p} \sum_{(\ell,m) \in \mathcal{S}_p} |\hat{y}_k[\ell, m] - h_k \cdot \hat{u}_k[\ell, m]|^2.$$

For the blind detector, in (21) we replace \mathcal{S}_p with the set of all index pairs (ℓ, m) , and we replace S_p with S ;

- Compute $R_a^{(b)}$ in (18) for each UE k by averaging, i.e., the rate for UE k is

$$R_{a,k}^{(b)} = \frac{1}{S} \sum_{(\ell,m) \notin \mathcal{S}_p} \log_2 \left(\frac{q_{\hat{u}_k, \hat{y}_k}(\hat{y}_k[\ell, m] | \hat{u}_k[\ell, m])^s}{\sum_a P(a) q_{\hat{u}_k, \hat{y}_k}(\hat{y}_k[\ell, m] | a)^s} \right) \tag{22}$$

where \hat{u}_k and \hat{y}_k are vectors collecting the $\hat{u}_k[\ell, m]$ and $\hat{y}_k[\ell, m]$, respectively, for all pairs (ℓ, m) . For the blind detector we set $\mathcal{S}_p = \emptyset$ in (22);

- Compute R_a in (17) for each UE, i.e., the average rate of UE k is $R_{a,k} = \frac{1}{B} \sum_{b=1}^B R_{a,k}^{(b)}$;
- Compute the average UE rate $\bar{R}_a = \frac{1}{K} \sum_{k=1}^K R_{a,k}$.

Our simulations showed that optimizing over $s \geq 0$ gives $s \approx 1$ if the channel parameters are chosen using (21).

4.2. Discussion

We make a few remarks on the lower bound. First, the receivers do not need to know α . Second, the rate R_a in (17) is achievable if one assumes stationarity and coding and decoding over many OFDM blocks. Third, as S grows, the channel estimate of the blind detector becomes more accurate and the performance approaches that of a coherent receiver. Related theory for PAT and large S is developed in [49]. However, the PAT rate is generally smaller than for a blind detector because the PAT channel estimate is less accurate and because PAT does not use all symbols for data.

Next, let $|\hat{\mathcal{U}}|$ be the number of elements in the modulation set $\hat{\mathcal{U}}$. The blind detector must generate $|\hat{\mathcal{U}}|^S$ likelihoods, which is prohibitively large unless $|\hat{\mathcal{U}}|$ and S are small. Moreover, the receiver must perform joint data and channel estimation. Blind detection algorithms can, e.g., be based on high-order statistics and iterative channel estimation and decoding. For polar codes and low-order constellations, one may use the blind algorithms proposed in [50]. We found that the PAT rates are very close (within 0.1 bpcu) of the pilot-free rates multiplied by the rate loss factor $1 - S_p/S$ for pilot fractions as small as $S_p/S = 10\%$.

Depending on the system under consideration, we choose one of $T_F = 32,256,396$, one of $T = 35,270,277,286,410$, one of $S = 256,1584$, and $B = 200$. For most simulations we have $T_F = S = 256$ and estimate the channel based on individual OFDM symbols, see Section 1.3. For example, for $T = 270$ and a symbol time of 30 ns (symbol rate 33.3 MHz) the coherence time needs to be at least $(30 \text{ ns}) \cdot T = 8.1 \mu\text{s}$. Of course, the transmitter needs to know the channel also, e.g., via time-division duplex, which requires the coherence time to be substantially larger. The main point is that channel estimation at the receiver is not a bottleneck when using ZF based on channel inversion. Finally, for the coded simulations we chose $T_F = 396$ and $S = 4T_F = 1548$ because the LDPC code occupies four OFDM symbols.

4.3. Algorithmic Complexity

This section studies the algorithmic complexity in terms of the number of multiplications and iterations. The complexity of SQUID is thoroughly discussed in [38] and Table 3 shows the order estimates take from [38] (Table I). Note the large number of iterations.

Table 3. Algorithmic complexity.

Algorithm	Multiplications per Iteration	Iterations	Pre-Processing Multiplications
QLP-ZF	$\mathcal{O}(TK^3 + TK^2N)$	1	-
SQUID	$\mathcal{O}(8KNT + 8NT \log T)$	20–300	$2T \cdot (\frac{5}{3}K^3 + 3K^2N + (6N - \frac{2}{3})K)$
MSM	$\mathcal{O}(4KNT^2 + 4KT + 2NT)$	≈ 8400	$4KNT$
MAGIQ & QCM	$\mathcal{O}(KNL + KNL \mathcal{X})$	4–6	$KNT + 4NT \log T$

The complexity of MSM depends on the choice of optimization algorithm and [42] considers a simplex algorithm. Unfortunately, the simplex algorithm requires a large number of iterations to converge because this number is proportional to the number of variables and linear inequalities that grow with the system size (N, K, T) . An interior point algorithm converges more quickly but has a much higher complexity per iteration.

For MAGIQ and QCM, Equation (8) shows that updating $x[\cdot]$ requires updating L of the T terms that each require a norm calculation. The resulting terms $\|\mathbf{u}[t]\|^2$ do not affect the maximization; terms such as $\|\alpha \mathbf{H} \mathbf{x}\|_2^2$ can be pre-computed and stored with a complexity of $NKL|\mathcal{X}|$, and then reused as they do not change during the iterations. On the other hand, products of the form $\alpha \mathbf{u}^H \mathbf{H} \mathbf{x}$ must be computed for each of the L terms for each antenna update and at each time instance, resulting in a complexity of $\mathcal{O}(NKLT)$. The initialization requires KNT multiplications and one must transform the solutions to the time domain. We neglect the cost of updating α because the terms needed to compute it are available as a byproduct of the iterative process over the time instances.

4.4. Sensitivity to Channel Uncertainty at the Transmitter

In practice, the CSI is imperfect due to noise, quantization, calibration errors, etc. We do not attempt to model these effects exactly. Instead, we adopt a standard approach based on MMSE estimation and provide the precoder with channel matrices $\tilde{\mathbf{H}}[\tau]$ that satisfy

$$\mathbf{H}[\tau] = \sqrt{1 - \varepsilon^2} \tilde{\mathbf{H}}[\tau] + \varepsilon \mathbf{Z}[\tau] \quad (23)$$

where $0 \leq \varepsilon \leq 1$ and $\mathbf{Z}[\tau]$ is a $K \times N$ matrix of independent, variance $\sigma_h^2 = 1/L$, complex, circularly-symmetric Gaussian entries. Note that $\varepsilon = 0$ corresponds to perfect CSI and $\varepsilon = 1$ corresponds to no CSI. The precoder treats $\tilde{\mathbf{H}}[\tau]$ as the true channel realization for $\tau = 0, \dots, L - 1$.

5. Numerical Results

We evaluate the GMIs of four systems. The main parameters are listed in Table 2 and we provide a few more details here.

- System A: the DFT has length $T_F = 256$ and the channel has either $L = 1$ or $L = 15$ taps of Rayleigh fading with a uniform PDP. The minimum cyclic prefix length for the latter case is $T_c = 14$ so the minimum OFDM blocklength is $T = 270$;
- System B: MSM is applied to PSK. However, the MSM complexity limited the simulations to smaller parameters than for System A. The channel now has $L = 4$ taps of Rayleigh fading with a uniform PDP. The $T = 35$ OFDM symbols include a DFT of length $T_F = 32$ and a minimum cyclic prefix length of $T_c = 3$;
- System C: System C is actually two systems because we compare the performance under Rayleigh fading to the performance with the Winner2 model [51] whose number L of channel taps varies randomly. For the Winner2 channel, the choice $T_c = 30$ suffices to ensure that $T_c \geq L - 1$. The Rayleigh fading model has $L = 22$ taps with a uniform PDP, where L was chosen as the maximum Winner2 channel length that has almost all the channel energy;
- System D: similar to System A but for a 5G NR LDPC code with code rate 8/9 and 64-QAM for an overall rate of 5.33 bpcu. The LDPC code uses the BG1 base graph

of the 3GPP Specification 38.212 Release 15, including puncturing and shortening as specified in the standard. The code length is 9504 bits or 1584 symbols of 64-QAM; this corresponds to 4 frames of $T_F = 396$ symbols. The codewords were transmitted using at least $T = 410$ symbols that include a DFT of length $T_F = 396$ and a minimum cyclic prefix length of $T_c = 14$.

The average GMIs for Systems A–C were computed using $S = 256$, $B = 200$, and a blind detector. The coded results of System D instead have $S = 1584$ symbols to fit the block structure determined by the LDPC encoder. For System D we considered both PAT and a blind detector. For all cases, the GMI was computed by averaging over the sub-carriers, i.e., channel coding is assumed to be applied over multiple sub-carriers and OFDM symbols. The MAGIQ and QCM algorithms were both initialized with a time-domain quantized solution of the transmit matched filter (MF).

Figures 3 and 4 show the average GMIs for System A with $b = 2$ and $b = 3$, respectively. In Figure 3, MAGIQ performs four iterations for each OFDM symbol while QCM performs six iterations. Observe that MAGIQ and QCM are best at all SNRs and they are especially good in the interesting regime of high SNR and rates. The gap to the rates over flat fading channels ($L = 1$) is small. SQUID with 64-QAM requires 100–300 iterations for $\text{SNR} > 15$ dB and a modified algorithm with damped updates, otherwise SQUID diverges. In addition, we show the broadcast channel capacity with uniform power allocation and Gaussian signaling as an upper bound for the considered scenario [52,53]. Figure 4 shows that QCM with three iterations operates within ≈ 0.2 – 0.4 dB of MAGIQ with five iterations when $b = 3$, which shows that QCM performs almost as well as MAGIQ.

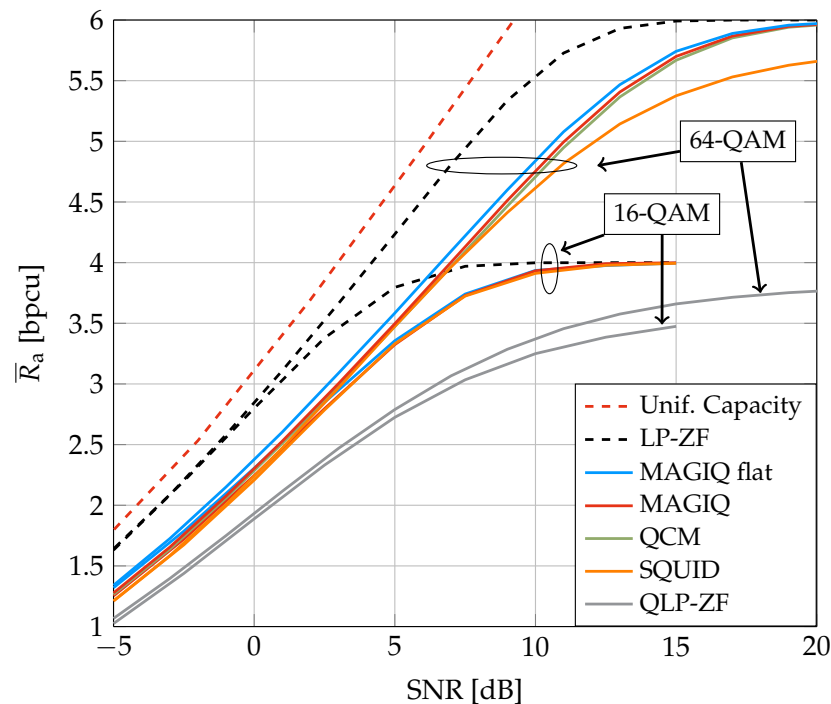


Figure 3. Average GMIs for System A and $b = 2$.

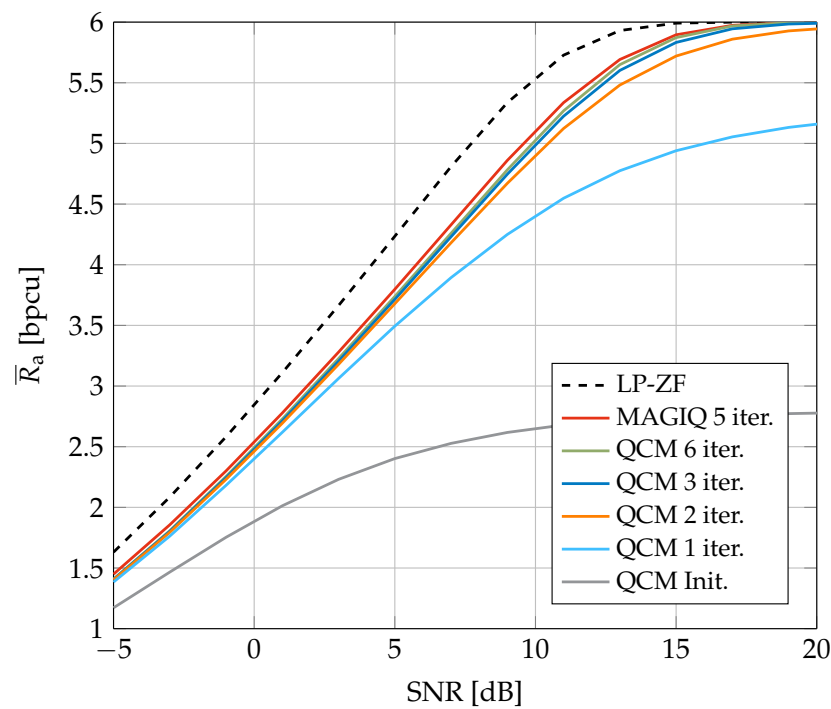


Figure 4. Average GMIs for System A with 64-QAM and $b = 3$.

Figure 5 compares achievable rates of QCM, SQUID, and MSM for a smaller system studied in [42]. We use PSK because the MSM algorithm was designed for PSK. The figure shows that MSM outperforms SQUID and QCM at low to intermediate SNR and rates, but QCM is best at high SNR and rates. This suggests that modifying the cost function (8) to include a safety margin will increase the QCM rate at low to intermediate SNR, and similarly modifying the MSM optimization to more closely resemble QCM will increase the MSM rate at high SNR. We tried to simulate MSM for System A but the algorithm ran into memory limitations (we used 2 AMD EPYC 7282 16-Core processors, 125 GB of system memory, and Matlab with both dual-simplex and interior-point solvers).

Consider next the Winner2 non-line-of-sight (NLOS) C2 urban model [51], which is more realistic than Rayleigh fading. The model parameters are as follows.

- Base station at the origin $(x, y) = (0, 0)$;
- 100 drops of 8 UEs placed on a disk of radius 150 m centered at $(x, y) = (0, 200 \text{ m})$; the locations of the UEs are iid with a uniform distribution on the disc;
- 8×10 uniform rectangular antenna array at the base station with half-wavelength dipoles at $\lambda/2$ spacing;
- 5 MHz bandwidth at center frequency 2.53 GHz;
- No Doppler shift, shadowing and pathloss.

Figure 6 shows the average GMIs for LP-ZF and MAGIQ. At high SNR, there is a slight decrease in the slope of the MAGIQ GMI as compared to LP-ZF. This suggests that one might need a larger N or b . The performance for the Rayleigh fading model is better than for the Winner2 model but otherwise behaves similarly.

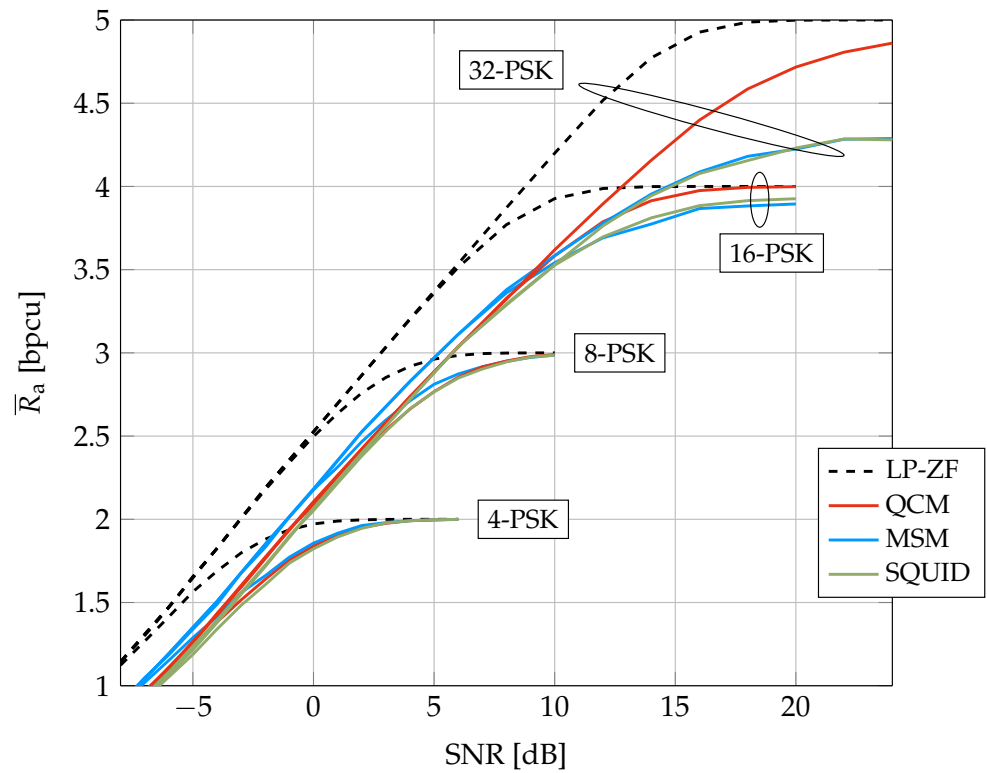


Figure 5. Average GMIs for System B.

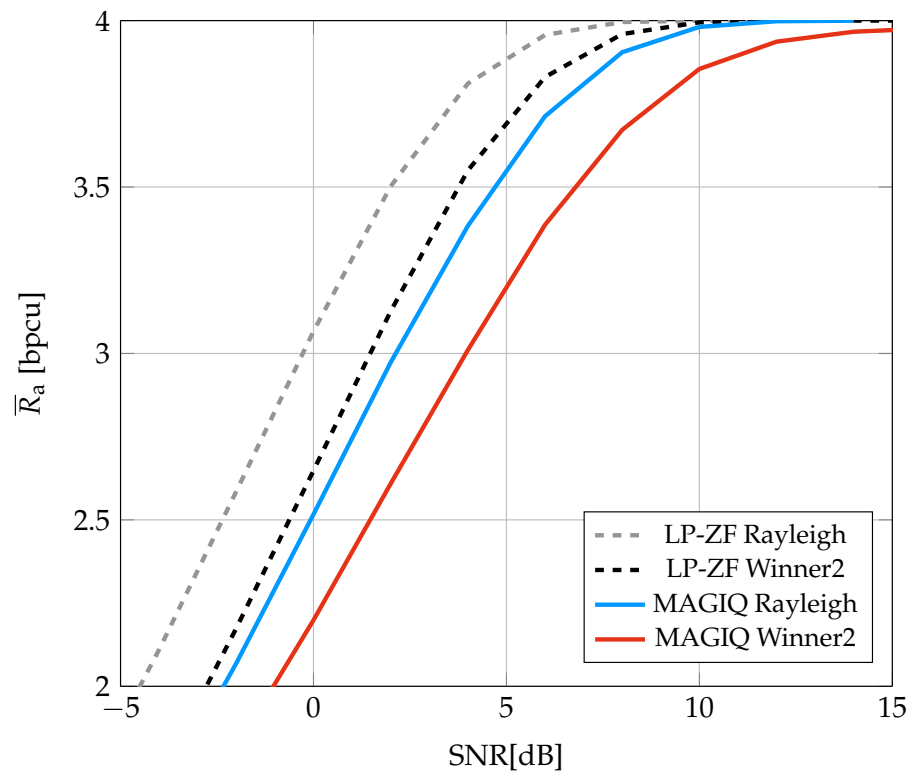


Figure 6. Average GMIs for System C.

Figure 7 shows BERs for the LDPC code with 64-QAM. Each codeword is interleaved over 4 OFDM symbols, all 396 subcarriers, and the 6 bits of each modulation symbol by using bit-interleaved coded modulation (BICM). The interleaver was chosen randomly with a uniform distribution over all permutations of length 9504. The solid curves are

based on estimating the channel with the transmitted symbols, i.e., these curves are for a genie-aided channel estimator and give lower bounds on the performance of a blind detector. The dotted curves show the performance of PAT when the fraction of pilots is $S_p/S = 10\%$. The pilots were placed uniformly at random over the four OFDM symbols and 396 subcarriers. A good blind detector algorithm that performs joint channel and data estimation should have BERs between the solid and dotted curves.

The dashed curves in Figure 7 show the SNRs required for the different algorithms based on Figure 3. In particular, the rate 5.33 bpcu requires SNRs of 9 dB, 12.9 dB, and 15.2 dB for LP-ZF, QCM, and SQUID, respectively. SQUID is run with 300 iterations and QCM is run with 6 iterations. Each UE computes its log-likelihoods based on the parameters (20) of the auxiliary channel. The GMI predicts the coded behavior of the system within approximately 1 dB of the code waterfall region, except for SQUID, where the gap is about 2 dB. The gap seems to be caused mainly by the finite-blocklength of the LDPC code, since the smaller gap of approximately 1 dB is also observed for additive white Gaussian noise (AWGN) channels. The sizes of the gaps are different, and the reason may be that the slopes of the GMI at rate 5.33 bpcu are different, see Figure 3. Observe that LP-ZF exhibits the steepest slope and SQUID the flattest at $R_a = 5.33$ bpcu; this suggests that SQUID's SNR performance is more sensitive to the blocklength.

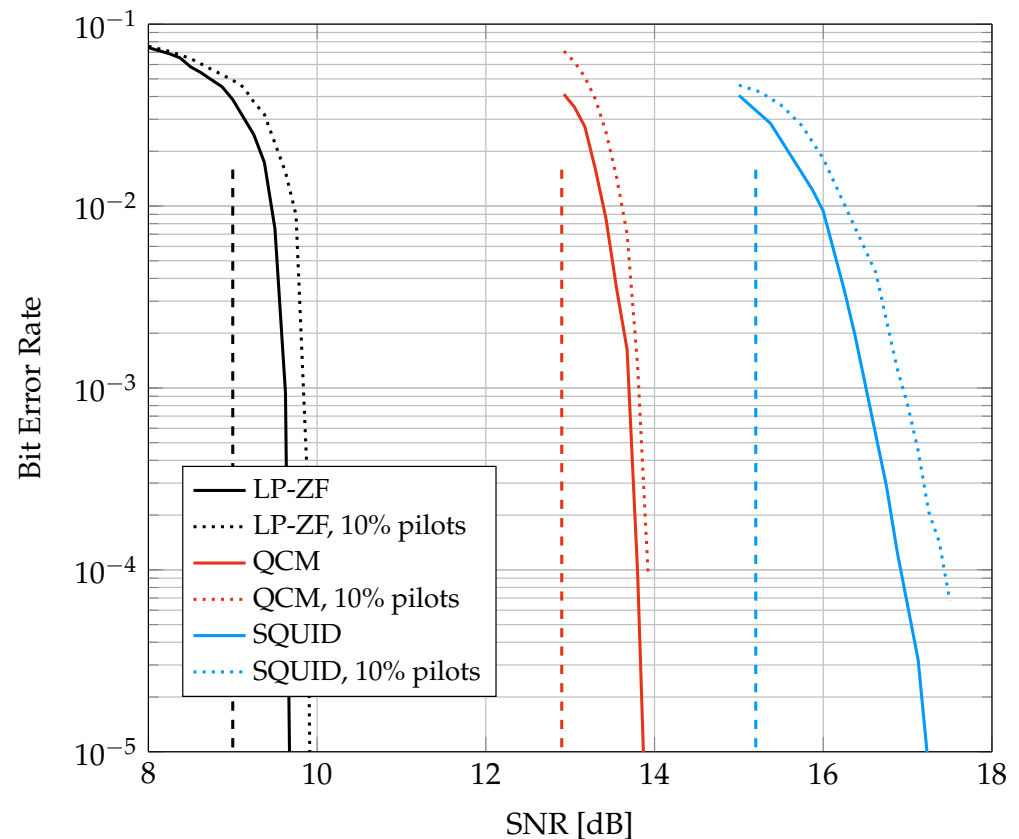


Figure 7. BERs for System D and a 5G NR LDPC code. The dashed vertical curves show the SNRs required for long random codes, see Figure 3.

Figure 8 is for System A and shows how the GMI decreases as the CSI becomes noisier. The behavior of all systems is qualitatively similar. However, the figure shows that the QCM rate is more sensitive to the parameter ϵ than the SQUID rate when ϵ is small.

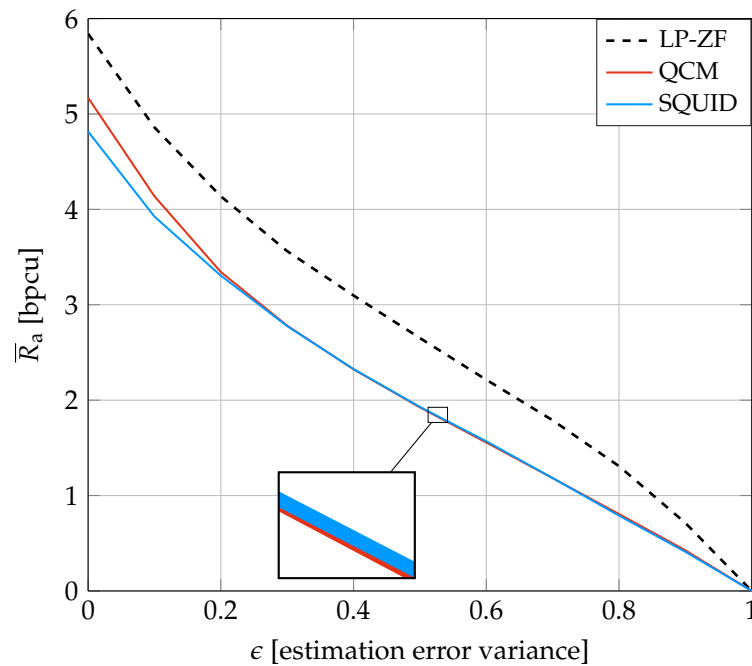


Figure 8. Average GMIs for System A and imperfect CSI at SNR = 12 dB.

6. Conclusions

We studied downlink precoding for MU-MISO channels where the base station uses OFDM and low-resolution DACs. A QCM algorithm was introduced that is based on the MAGIQ algorithm in [39] (see also [19]) and which performs a coordinate-wise optimization in the time-domain. The performance was analyzed by computing the GMI for two auxiliary channel models: one model for pilot-aided channel estimation and a second model for a blind detector that performs joint channel and data estimation. Simulations for several downlink channels, including a Winner2 NLOS urban scenario, showed that QCM achieves high information rates and is computationally efficient, flexible, and robust. The performance of QCM was compared to MAGIQ and other precoding algorithms including SQUID and MSM. The QCM and MAGIQ algorithms achieve the highest information rates with the lowest complexity measured by the number of multiplications. For example, Figure 4 shows that $b = 3$ bits of phase modulation operates within 3 dB of LP-ZF. Moreover, BER simulations for a 5G NR LDPC code show that GMI is a good predictor of the coded performance. Finally, for noisy CSI the performance degradation of QCM and SQUID is qualitatively similar to the performance degradation of LP-ZF.

Author Contributions: Investigation, A.S.N., F.S. and G.K.; Software, A.S.N.; Writing—original draft, F.S.; Writing—review & editing, A.S.N. and G.K. All authors have read and agreed to the published version of the manuscript.

Funding: This research was funded by Deutsche Forschungsgemeinschaft through the grant KR 3517/9-1, and by Nokia Solutions and Networks through the project “Low Cost Booster Arrays for Massive MIMO Precoding” in 2017.

Acknowledgments: The authors wish to thank M. Staudacher, W. Zirwas, B. Panzner, R. S. Ganesan, P. Baracca, and S. Wesemann for useful discussions.

Conflicts of Interest: The authors declare no conflict of interest.

References

1. Marzetta, T. Noncooperative cellular wireless with unlimited numbers of base station antennas. *IEEE Trans. Wirel. Commun.* **2010**, *9*, 3590–3600. [[CrossRef](#)]
2. Ngo, H.Q.; Larsson, E.; Marzetta, T. Energy and spectral efficiency of very large multiuser MIMO systems. *IEEE Trans. Commun.* **2013**, *61*, 1436–1449.
3. Mohammed, S.K.; Larsson, E.G. Per-antenna constant envelope precoding for large multi-user MIMO systems. *IEEE Trans. Commun.* **2013**, *61*, 1059–1071. [[CrossRef](#)]
4. Mohammed, S.K.; Larsson, E.G. Constant-envelope multi-user precoding for frequency-selective massive MIMO systems. *IEEE Wirel. Commun. Lett.* **2013**, *2*, 547–550. [[CrossRef](#)]
5. Mohammed, S.K.; Larsson, E.G. Single-User beamforming in large-scale MISO systems with per-antenna constant-envelope constraints: The doughnut channel. *IEEE Trans. Wirel. Commun.* **2012**, *11*, 3992–4005. [[CrossRef](#)]
6. Joham, M.; Utschick, W.; Nossek, J.A. Linear transmit processing in MIMO communications systems. *IEEE Trans. Signal Process.* **2005**, *53*, 2700–2712. [[CrossRef](#)]
7. Björnson, E.; Bengtsson, M.; Ottersten, B. Optimal multiuser transmit beamforming: A difficult problem with a simple solution structure. *IEEE Signal Proc. Mag.* **2014**, *31*, 142–148.
8. Mezghani, A.; Ghat, R.; Nossek, J.A. Transmit processing with low resolution D/A-converters. In Proceedings of the 2009 16th IEEE International Conference on Electronics, Circuits and Systems—(ICECS 2009), Yasmine Hammamet, Tunisia, 13–16 December 2009.
9. Mezghani, A.; Ghat, R.; Nossek, J.A. Tomlinson Harashima Precoding for MIMO Systems with Low Resolution D/A-Converters. In Proceedings of the ITG/IEEE Workshop on Smart Antennas, Berlin, Germany, 18–20 February 2009.
10. Usman, O.B.; Jedda, H.; Mezghani, A.; Nossek, J.A. MMSE precoder for massive MIMO using 1-bit quantization. In Proceedings of the 2016 IEEE International Conference on Acoustics, Speech and Signal Processing (ICASSP), Shanghai, China, 20–25 March 2016.
11. Saxena, A.K.; Fijalkow, I.; Swindlehurst, A.L. Analysis of one-bit quantized precoding for the multiuser massive MIMO downlink. *IEEE Trans. Signal Proc.* **2017**, *65*, 4624–4634. [[CrossRef](#)]
12. Kakkavas, A.; Munir, J.; Mezghani, A.; Brunner, H.; Nossek, J.A. Weighted sum rate maximization for multi-user MISO systems with low resolution digital to analog converters. In Proceedings of the International ITG Workshop Smart Antennas, Munich, Germany, 9–11 March 2016.
13. Li, Y.; Tao, C.; Swindlehurst, A.; Mezghani, A.; Liu, L. Downlink achievable rate analysis in massive MIMO systems with one-bit DACs. *IEEE Commun. Lett.* **2017**, *21*, 1669–1672. [[CrossRef](#)]
14. Swindlehurst, A.; Jedda, H.; Fijalkow, I. Reduced dimension minimum BER PSK precoding for constrained transmit signals in massive MIMO. In Proceedings of the 2018 IEEE International Conference on Acoustics, Speech and Signal Processing (ICASSP), Calgary, AB, Canada, 15–20 April 2018.
15. Saxena, A.K.; Mezghani, A.; Heath, R.W. Linear CE and 1-bit quantized precoding with optimized dithering. *IEEE Open J. Signal Proc.* **2020**, *1*, 310–325. [[CrossRef](#)]
16. Jedda, H.; Nossek, J.A.; Mezghani, A. Minimum BER precoding in 1-bit massive MIMO systems. In Proceedings of the 2016 IEEE Sensor Array and Multichannel Signal Processing Workshop (SAM), Rio de Janeiro, Brazil, 10–13 July 2016.
17. Jacobsson, S.; Durisi, G.; Coldrey, M.; Goldstein, T.; Studer, C. Quantized precoding for massive MU-MIMO. *IEEE Trans. Commun.* **2017**, *65*, 4670–4684. [[CrossRef](#)]
18. Wang, C.-J.; Wen, C.-K.; Jin, S.; Tsai, S.-H. Finite-alphabet precoding for massive MU-MIMO with low-resolution DACs. *IEEE Trans. Wirel. Commun.* **2018**, *17*, 4706–4720. [[CrossRef](#)]
19. Staudacher, M.; Kramer, G.; Zirwas, W.; Panzner, B.; Ganesan, R.S. Optimized combination of conventional and constrained massive MIMO arrays. In Proceedings of the ITG Workshop Smart Antennas, Berlin, Germany, 15–17 March 2017; pp. 1–4.
20. Shao, M.; Li, Q.; Ma, W.-K. One-bit massive MIMO precoding via a minimum symbol-error probability design. In Proceedings of the 2018 IEEE International Conference on Acoustics, Speech and Signal Processing (ICASSP), Calgary, AB, Canada, 15–20 April 2018.
21. Tsinos, C.G.; Kalantari, A.; Chatzinotas, S.; Ottersten, B. Symbol-level precoding with low resolution DACs for large-scale array MU-MIMO systems. In Proceedings of the 2018 IEEE 19th International Workshop on Signal Processing Advances in Wireless Communications (SPAWC), Kalamata, Greece, 25–28 June 2018; pp. 1–5.
22. Domouchtsidis, S.; Tsinos, C.; Chatzinotas, S.; Ottersten, B. Symbol-level precoding for low complexity transmitter architectures in large-scale antenna array systems. *IEEE Trans. Wirel. Commun.* **2019**, *18*, 852–863. [[CrossRef](#)]
23. Li, A.; Masouros, C.; Liu, F.; Swindlehurst, A.L. Massive MIMO 1-Bit DAC transmission: A low-complexity symbol scaling approach. *IEEE Trans. Wirel. Commun.* **2018**, *17*, 7559–7575. [[CrossRef](#)]
24. Li, A.; Masouros, C.; Swindlehurst, A.L.; Yu, W. 1-Bit massive MIMO transmission: Embracing interference with symbol-level precoding. *IEEE Commun. Mag.* **2021**, *59*, 121–127. [[CrossRef](#)]
25. Li, A.; Liu, F.; Liao, X.; Shen, Y.; Masouros, C. Symbol-level precoding made practical for multi-level modulations via block-level rescaling. In Proceedings of the IEEE International workshop on Signal Processing advances in Wireless Communications, Oulu, Finland, 4–6 July 2022; pp. 71–75.

26. Jedda, H.; Mezghani, A.; Nossek, J.A.; Swindlehurst, A.L. Massive MIMO downlink 1-bit precoding with linear programming for PSK signaling. In Proceedings of the 2017 IEEE 18th International Workshop on Signal Processing Advances in Wireless Communications (SPAWC), Sapporo, Japan, 3–6 July 2017; pp. 1–5.
27. Jedda, H.; Mezghani, A.; Swindlehurst, A.L.; Nossek, J.A. Quantized constant envelope precoding with PSK and QAM signaling. *IEEE Trans. Wirel. Commun.* **2018**, *17*, 8022–8034. [[CrossRef](#)]
28. Jedda, H.; Mezghani, A.; Nossek, J.A.; Swindlehurst, A.L. Massive MIMO downlink 1-bit precoding for frequency selective channels. In Proceedings of the 2017 IEEE 7th International Workshop on Computational Advances in Multi-Sensor Adaptive Processing (CAMSAP), Curacao, 10–13 December 2017.
29. Landau, L.T.N.; de Lamare, R.C. Branch-and-bound precoding for multiuser MIMO systems with 1-bit quantization. *IEEE Wirel. Commun. Lett.* **2017**, *6*, 770–773. [[CrossRef](#)]
30. Jacobsson, S.; Xu, W.; Durisi, G.; Studer, C. MSE-optimal 1-bit precoding for multiuser MIMO via branch and bound. In Proceedings of the 2018 IEEE International Conference on Acoustics, Speech and Signal Processing (ICASSP), Calgary, AB, Canada, 15–20 April 2018.
31. Li, A.; Liu, F.; Masouros, C.; Li, Y.; Vucetic, B. Interference exploitation 1-bit massive MIMO precoding: A partial branch-and-bound solution with near-optimal performance. *IEEE Trans. Wirel. Commun.* **2020**, *19*, 3474–3489. [[CrossRef](#)]
32. Lopes, E.S.P.; Landau, L.T.N. Optimal and suboptimal MMSE precoding for multiuser MIMO systems using constant envelope signals with phase quantization at the transmitter and PSK. In Proceedings of the International ITG Workshop on Smart Antennas, WSA 2020, Hamburg, Germany, 18–20 February 2020; pp. 1–6.
33. Shao, M.; Li, Q.; Ma, W.; So, A.M.; A framework for one-bit and constant-envelope precoding over multiuser massive MISO channels. *IEEE Trans. Sig. Proc.* **2019**, *67*, 5309–5324. [[CrossRef](#)]
34. Sedaghat, M.A.; Beryhi, A.; Müller, R.R. Least square error precoders for massive MIMO With signal constraints: Fundamental limits. *IEEE Trans. Wirel. Commun.* **2018**, *17*, 667–679. [[CrossRef](#)]
35. Balatsoukas-Stimming, A.; Castañeda, C.; Jacobsson, S.; Durisi, G.; Studer, C. Neural-network optimized 1-bit precoding for massive MU-MIMO. In Proceedings of the 2019 IEEE 20th International Workshop on Signal Processing Advances in Wireless Communications (SPAWC), Cannes, France, 2–5 July 2019; pp. 1–5.
36. Sohrabi, F.; Cheng, H.V.; Yu, W. Robust symbol-level precoding via autoencoder-based deep learning. In Proceedings of the ICASSP 2020—2020 IEEE International Conference on Acoustics, Speech and Signal Processing (ICASSP), Barcelona, Spain, 4–8 May 2020; pp. 8951–8955.
37. Jacobsson, S.; Durisi, G.; Coldrey, M.; Studer, C. Linear precoding with low-resolution DACs for massive MU-MIMO-OFDM downlink. *IEEE Trans. Wirel. Commun.* **2019**, *18*, 1595–1609. [[CrossRef](#)]
38. Jacobsson, S.; Castañeda, C.O.; Jeon, D.G.; Studer, C. Nonlinear precoding for phase-quantized constant-envelope massive MU-MIMO-OFDM. In Proceedings of the International Conference on Telecommunications and Communication Engineering, Beijing China, 28–30 November 2018; pp. 367–372.
39. Nedelcu, A.; Steiner, F.; Staudacher, M.; Kramer, G.; Zirwas, W.; Ganesan, R.S.; Baracca, P.; Wesemann, S. Quantized precoding for multi-antenna downlink channels with MAGIQ. In Proceedings of the International ITG Workshop on Smart Antennas, WSA 2018, Bochum, Germany, 14–16 March 2018; pp. 1–8.
40. Tsinos, C.G.; Domouchtsidis, S.; Chatzinotas, S.; Ottersten, B. Symbol level precoding with low resolution DACs for constant envelope OFDM MU-MIMO systems. *IEEE Access* **2020**, *8*, 12856–12866. [[CrossRef](#)]
41. Domouchtsidis, S.; Tsinos, C.G.; Chatzinotas, S.; Ottersten, B. Joint symbol level precoding and combining for MIMO-OFDM transceiver architectures based on one-bit DACs and ADCs. *IEEE Trans. Wirel. Commun.* **2021**, *20*, 4601–4613. [[CrossRef](#)]
42. Askerbeyli, F.; Jedda, H.; Nossek, J.A. 1-bit precoding in massive MU-MISO-OFDM downlink with linear programming. In Proceedings of the International ITG Workshop on Smart Antennas, WSA 2019, Vienna, Austria, 24–26 April 2019; pp. 1–5.
43. Mezghani, A.; Heath, R.W. Massive MIMO precoding and spectral shaping with low resolution phase-only DACs and active constellation extension. *IEEE Trans. Wirel. Commun.* **2022**. [[CrossRef](#)]
44. Bae, J.H.; Abotabl, A.; Lin, H.-P.; Song, K.-B.; Lee, J. An overview of channel coding for 5G NR cellular communications. *APSIPA Trans. Signal Inf. Proc.* **2019**, *8*, e17. [[CrossRef](#)]
45. Zhang, J.; Huang, Y.; Wang, J.; Ottersten, B.; Yang, L. Per-antenna constant envelope precoding and antenna subset selection: A geometric approach. *IEEE Trans. Signal Process.* **2016**, *64*, 6089–6104. [[CrossRef](#)]
46. Kaplan, G.; Shamai, S. Information rates and error exponents of compound channels with application to antipodal signaling in a fading environment. *AEU. Archiv Elektr. Übertrag.* **1993**, *47*, 228–239.
47. Gallager, R.G. *Information Theory and Reliable Communication*; John Wiley & Sons, Inc.: Hoboken, NJ, USA, 1968.
48. Arnold, D.M.; Loeliger, H.A.; Vontobel, P.O.; Kavcic, A.; Zeng, W. Simulation-based computation of information rates for channels with memory. *IEEE Trans. Inf. Theory* **2006**, *52*, 3498–3508. [[CrossRef](#)]
49. Meng, X.; Gao, K.; Hochwald, B.M. A training-based mutual information lower bound for large-scale systems. *arXiv* **2021**, arXiv:2108.00034.
50. Yuan, P.; Coşkun, M.C.; Kramer, G. Polar-coded non-coherent communication. *IEEE Commun. Lett.* **2021**, *25*, 1786–1790. [[CrossRef](#)]
51. Kyösti, P. IST-4-027756 WINNER II D1.1.2 V1.2. 2007. Available online: <https://www.cept.org/files/8339/winner2%20-%20ofinal%20report.pdf> (accessed on 1 February 2022).

-
52. Viswanath, P.; Tse, D.N.C. Sum capacity of the vector Gaussian broadcast channel and downlink-uplink duality. *IEEE Trans. Inf. Theory* **2003**, *49*, 1912–1921. [[CrossRef](#)]
 53. Vishwanath, S.; Jindal, N.; Goldsmith, A. Duality, achievable rates and sum rate capacity of Gaussian MIMO broadcast channel. *IEEE Trans. Inf. Theory* **2003**, *49*, 2658–2668. [[CrossRef](#)]